LONG-TERM MONITORING OF COMET 103P/HARTLEY 2*

Z.-Y. LIN[1], L. M. LARA[2], AND W.-H. IP[1]

[1] Institute of Astronomy, National Central University, Jhongli City, Taoyuan County 32001,
Taiwan, Taiwan; zylin@astro.ncu.edu.tw

[2] Instituto de Astrofísica de Andalucía (CSIC), Glorieta de la Astronomía s/n, ES-18008 Granada, Spain; lara@iaa.csic.es

ABSTRACT

We report the spectrophotometric, photometric, and imaging monitoring results of comet 103P/Hartley 2 obtained at the Lulin (1 m), Calar Alto (2.2 m), and Beijing Astronomical (2.16 m) observatories from 2010 April to December. We found that a dust feature in the sunward direction was detected starting from the end of September until the beginning of December (our last observation from the Lulin and Calar Alto observatories). Two distinct sunward jet features in the processed images were observed on October 11 and after October 29 until November 2. In parallel, the CN images reveal two asymmetrical jet features which are nearly perpendicular to the Sun-nucleus direction, these asymmetrical features imply that the comet was in a nearly side-on view in late October and early November. In addition to the jet features, the average result of the C_2-to-CN production rate ratio ranges from 0.7 to 1.5, consistent with 103P/Hartley 2 being of typical cometary chemistry. We found that the r_h dependence for the dust production rate, Afρ (5000 km), is -3.75 ± 0.45 before perihelion and -3.44 ± 1.20 during the post-perihelion period. We detected higher dust reddening around the optocenter and decreased reddening along the sunward jet feature. We concluded that higher dust reddening could be associated with strong jet activity while lower dust reddening could be associated with the outburst or might imply changes in the optical properties. The average dust color did not appear to vary significantly as the comet passed through perihelion.

Key words: comets: individual (103P/Hartley 2) – dust, extinction

Online-only material: color figures

1. INTRODUCTION

Comet 103P/Hartley 2, hereafter referred to as Hartley 2, was first spotted by M. Hartley on 1986 March 16. It has a semimajor axis of $a = 3.47$ AU, eccentricity $e = 0.695$, inclination $i = 13.617$, and an orbital period of 6.46 yr. Its low eccentricity made it a suitable target for the extended mission of NASA's *Deep Impact* spacecraft after the impact experiment at comet 9P/Tempel 1 on 2005 July 4. The mission to Hartley 2 was renamed *EPOXI* and given two missions, Extrasolar Planet Observation and Characterization and Deep Impact Extended Investigation. The *EPOXI* flyby observations at a closest distance of 694 km on 2010 November 4 provided a wealth of information on the outgassing activity, shape, and surface structure of this small Jupiter-family comet (A'Hearn et al. 2011). For example, the strong outflows of the CO_2-rich jet from the Sun-lit end of the bowling-pin shape and the H_2O-rich jet in the waist region came as surprises. How are these out flows connected to the large-scale jet structures observed in the coma? How would the outgassing process be modulated by the rotation of the comet nucleus? In fact, based on the time variability of the CN coma morphology and millimeter/submillimeter spectra, the rotation period of Hartley 2 has been found to be increasing from 16.7 hr in 2010 August to 18.4 hr in the first half of November and then to nearly 19 hr in late November (Drahus et al. 2011; Samarasinha et al. 2011; Knight & Schleicher 2011; Meech et al. 2011; Waniak et al. 2012). Such time variations of the nucleus rotation period,

together with the close-up measurements from the *EPOXI* mission, demonstrate the complex nature of the surface outgassing process.

In anticipation of the scientific opportunity to compare the large-scale coma structures and gas production rates of Hartley 2 with the *EPOXI* results, we conducted a long-term monitoring program from 2010 April to December using imaging with both broadband and narrowband filters, and long-slit spectrophotometry. This cooperative effort involved observations at the Lulin Observatory in Taiwan, the Calar Alto Observatory in Spain, and the Beijing Astronomical Observatory in China. The paper is organized as follows. In Section 2, we explain the observational procedures, instruments, and analysis methods. In Section 3, the derived morphology and gas production of the CN coma and jets are described. In Section 4, we describe the dust jets and the structure of the dust coma during this period. A summary of the major characteristics of the large-scale structures of the gas and dust comas of Hartley 2 is given in Section 5.

2. OBSERVATIONS, INSTRUMENTS, AND DATA ANALYSIS

Imaging. The bulk of the photometric imaging observations was done using the Lulin One-meter Telescope (LOT) at Lulin Observatory. In our first image of Hartley 2 on 2010 April 24 when the comet was 2.42 AU away from the Sun and 2.36 AU from the Earth, only a diffuse coma 5″ in diameter was visible in a 10 minute exposure. There was no tail feature. In the monitoring program, an Asahi *R* broadband filter and the narrowband filters of the *Rosetta* filter set were used. The specifications of these narrowband filters are given as $\lambda_c/\Delta\lambda$ both in nm, λ_c being the central wavelength and $\Delta\lambda$ the band width: CN (387/5 nm), C_2 (512.5/12.5 nm), blue continuum

Table 1
Log of Observations

Date	UT	r_h	Δ	PA	α	Pix Scale	Data	Obs.	Sky
Apr 24	19:56–20:17	2.424	2.363	256.2	24.2	884.4	R	Lulin	Phot.
May 11	18:39–18:48	2.283	2.026	252.1	26.3	758.2	R	Lulin	Phot.
May 15	18:58–19:10	2.249	1.948	251.0	26.7	729.1	R	Lulin	Part. cloudy
May 16	19:07–19:36	2.240	1.928	250.8	26.8	721.6	R	Lulin	Part. cloudy
May 20	18:34–18:56	2.206	1.851	249.7	27.1	692.7	R	Lulin	Part. cloudy
Jul 14	17:01–18:40	1.721	0.924	226.9	29.0	345.8	R	Lulin	Part. cloudy
Jul 14	23:00–23:49	1.719	0.921	226.7	29.0	354.0	R	CA	Phot.
Jul 22	01:25–02:36	1.656	0.825	221.7	29.0	316.1	R	CA	Part. phot.
Jul 30	02:22–02:55	1.585	0.725	215.2	29.2	278.7	R	CA	Phot.
Aug 1	17:30–18:42	1.562	0.694	212.9	29.3	259.7	R	Lulin	Phot.
Aug 19	14:00–20:15	1.409	0.503	195.5	31.1	188.3	R	Lulin	Part. cloudy
Aug 20	01:33–01:44	1.406	0.500	195.1	31.1	192.2	R	CA	Phot.
Aug 20	13:17–20:01	1.402	0.494	194.5	31.2	184.9	R	Lulin	Phot.
Aug 21	19:27–20:43	1.392	0.483	193.3	31.4	180.8	R	Lulin	Phot.
Aug 25	22:46–00:23	1.359	0.445	189.3	32.3	174.5	R, S	CA	Phot.
Aug 29	18:37–19:09	1.329	0.412	185.6	33.3	154.2	R	Lulin	Part. cloudy
Sep 2	02:23–02:27	1.304	0.384	182.7	34.2	147.6	R, S	CA	Part. phot.
Sep 14	00:35–00:57	1.219	0.293	175.1	38.3	109.2	R, S	CA	Phot.
Sep 29	14:45–20:51	1.130	0.192	182.1	44.2	71.9	R	Lulin	Phot.
Sep 30	13:55–20:06	1.125	0.186	183.8	44.6	69.6	R	Lulin	Phot.
Oct 2	17:55–18;05	1.116	0.175	188.3	45.3	65.5	R	Lulin	Part. phot.
Oct 3	15:21–15:30	1.112	0.170	191.1	45.6	63.6	R	Lulin	Part. phot.
Oct 9	14:40–17:55	1.090	0.143	211.7	47.7		S	BAO	Part. phot.
Oct 10	12:32–18:45	1.087	0.140	215.9	48.0	52.4	R+N	Lulin	Phot.
Oct 11	15:08–19:00	1.083	0.136	220.3	48.4		S	BAO	Phot.
Oct 11	13:05–21:08	1.083	0.136	220.3	48.4	50.9	R+N	Lulin	Phot.
Oct 15	00:28–02:18	1.077	0.129	230.9	49.4	48.8	R, S	CA	Part. cloudy
Oct 18	04:38–05:10	1.068	0.122	248.1	51.4	46.9	R, S	CA	Phot.
Oct 19	22:32–23:15	1.065	0.121	254.4	52.5	46.5	R, S	CA	Part. phot.
Oct 22	02:39–03:13	1.062	0.121	261.0	53.8	46.5	R, S	CA	Phot.
Oct 25	03:53–04:38	1.060	0.125	268.6	55.6	47.6	R	CA	Part. cloudy
Oct 25	18:09–18:39	1.059	0.126	269.8	55.9	47.2	R+N	Lulin	Phot.
Oct 26	16:09–21:24	1.059	0.128	271.8	56.4	47.9	N	Lulin	Phot.
Oct 27	16:24–26:56	1.059	0.130	273.7	56.5	48.7	N	Lulin	Phot.
Oct 28	17:50–21:28	1.059	0.132	275.3	57.4	49.4	N	Lulin	Phot.
Oct 29	03:06–03:20	1.059	0.133	275.9	57.5	51.1	R	CA	Part. cloudy
Oct 29	16:24–21:00	1.059	0.135	276.9	57.7	50.5	R+N	Lulin	Phot.
Nov 1	19:14–21:12	1.060	0.145	280.9	58.6	54.3	R	Lulin	Part. cloudy
Nov 2	17:58–20:31	1.061	0.150	282.0	58.7	56.1	R+N	Lulin	Phot.
Nov 3	16:04–16:28	1.061	0.149	281.9	58.7	55.7	R	Lulin	Part. cloudy
Nov 5	18:07–21:09	1.064	0.157	284.2	58.8	58.8	R	Lulin	Part. cloudy
Nov 5	01:25–05:45	1.065	0.162	285.4	58.8	62.3	R, S	CA	Part. phot.
Nov 16	01:18–01:47	1.090	0.210	294.0	56.1	80.3	R, S	CA	Part. phot.
Nov 21	19:07–19:37	1.112	0.239	298.8	53.2	60.3	R	Lulin	Phot.
Dec 2	16:24–18:48	1.116	0.295	308.9	46.4	74.5	R	Lulin	Part. cloudy
Dec 17	17:48–20:58	1.262	0.377	326.2	36.4	95.2	R	Lulin	Phot.
Dec 26	23:08–00:12	1.323	0.427	338.0	31.3	163.7	R, S	CA	Phot.

Notes. Δ and r_h are the geocentric and heliocentric distances in AU; PA is the extended Sun-target radius vector as seen in the observer's plane-of-sky, measured from north toward east. α is the phase angle (Sun-comet-observer angle). R is the broadband filter, N is the cometary filter set, and S refers to long-slit spectra.

(BC; 443/4 nm), and red continuum (RC; 684/9 nm). Because of the consideration of the signal-to-noise ratio (S/N), the narrowband filters were used only in October and on November 2 just before the *EPOXI* close encounter. The camera used on LOT from April to November was PI 1300B, which has a pixel scale of 0.516 arcsec and a field of view (FOV) of 11.2×11.6 arcmin. In 2010 late November, there was a cooling problem with PI1300B. We therefore switched to a U42 CCD which has $2k \times 2k$ pixels and a FOV of 12.17×11.88 arcmin. The telescope was always operated with non-sidereal tracking so as not to produce a trail in the comet images. Typical integrations were 600 s–900 s for the narrowband filters and 30 s–300 s for the broadband *R* filter.

Table 1 is the observational log of our program. Standard data reduction procedures were applied, beginning with dark current subtraction and a flat-field correction of all image frames and followed by the subtraction of the night sky contribution. For the observations obtained before late September, the night sky levels were determined directly from areas of the CCD frames that did not contain contributions from the cometary emission. However, the sky-background of those images taken from late-September to early-November was influenced by the

cometary coma. Therefore, we took sky background images positioned about 0.5 deg away from the comet center. The extinction coefficients of the narrowband and broadband R filters were determined for all nights with photometric sky conditions, using photometric stars like Feige 110 and GD71 observed at different air masses during the night. For example, the first order extinction coefficient (in units of magnitudes per air mass) measured with Feige 110 at air masses ranging from 1.1 to 1.7 for the R filter on October 29 is 0.10. For the CN and C_2 filters, the corresponding values are 0.39 and 0.14, respectively. These data were used to convert the measured counting rates into physical units; details are described in Lin et al. (2007b). Because the CN images contain a 29% contribution from the continuum in the blue range while the C_2 images contain as much as a 93% contribution, the net CN and C_2 gas coma images need to go through the subtraction procedure according to the following formulas: $CN = CN_{obs} - 0.29\, BC_{obs}$, $C_2 = C_2^{obs} - 0.93\, BC_{obs}$.

In addition to the Lulin observations, the coma activity of 103P/Hartley 2 was also monitored continuously in the R-band from the Calar Alto Observatory (near Almeria, Spain) from 2010 July 14 to December 26 (see Table 1). We used the CAFOS imaging camera (2k × 2k pixels, pixel size: $0\rlap{.}''53$, FOV $18' \times 18'$), which was mounted on the 2.2 m telescope. In our observations, only the central 1k × 1k pixels were used, thus providing an FOV of $9' \times 9'$. Appropriate bias and flat field frames were taken each night. If photometric conditions prevailed, photometric standard stars were observed at air masses similar to those of the comet observations. Table 1 contains the observations log for the complete data set. Note that a large number of nights listed in Table 1 were used for the Afρ estimation; some of these nights were not used to enhance the structures in the coma because the S/N was too low.

Spectroscopy. Spectroscopic measurements were planned once every month using CAFOS with the B400 grism (see http://www.caha.es/alises/cafos/cafos22.pdf) which renders a spectral range between 3200 and 8800 Å with a wavelength scale of 9.4 Å pixel^{-1}. The slit of the spectrograph was oriented in the north–south direction, giving dust and gas profiles at different cross-cuts through the coma, depending on the position angle (PA) of the Sun-comet vector on the sky. For absolute calibration, observations of appropriate spectrophotometric standard stars were acquired. All comet observations were done with telescope tracking on Hartley 2. With the exception of 2010 November 5, all observations were done in service mode of the Calar Alto Observatory. Details on the images and spectra reduction and calibration can be found in Lara et al. (2001, 2011b) and they will not be repeated here. If the gas coma covered the whole slit, the sky level was estimated from the edges of the frame. Otherwise, the background could be measured directly by using regions near the edges of the frame.

Besides spectra obtained from the Calar Alto Observatory, spectroscopic observations were also performed on October 9 and October 11 at the Beijing Astronomical Observatory using the 2.16 m telescope in the spectral range between 3600 Å and 8400 Å at a dispersion of 4.8 Å pixel^{-1}. The spectroscopic data were reduced following the standard procedures including bias and flat-field corrections and cosmic ray removal. Wavelength calibration was performed based on helium–argon lamps exposed at both the beginning and the end of the observations every night. Flux calibration of all spectra was conducted based on observations of at least one of the spectral standard stars, i.e., HD19445. The atmospheric extinction effect was corrected by the mean extinction coefficients measured by the

Beijing–Arizona–Taiwan–Connecticut multicolor survey. See Lin et al. (2007a) for more detailed information.

3. GAS COMA MORPHOLOGY AND PROPERTIES

3.1. CN Jets

In order to study the visibility of faint structures of the gas coma of comet Hartley 2, an image enhancement technique was applied to the present set of images. The method used here is the azimuthally averaged profile division, a detailed description of which can be found in Lin et al. (2012). This method was applied to all images taken in the CN filter, in continuum filters, and in the R-band filter.

To estimate the rotational phase from the CN morphology, a lot of observing data have to be acquired on consecutive nights. However, the images obtained in our observing nights with less temporal coverage were not enough to estimate and display the rotational period due to snapshot observations, poor weather, and telescope tracking problems. We therefore use the known periodicity to estimate the rotational phase in our images. However, we face several problems: a non-principal axis rotation of comet Hartley 2 and a rapid change of the viewing geometry might cause different periodicities between rotational cycles. A specific phase is really only applicable to a short stretch of data if we adopt a known periodicity such as 18.15 hr in mid-October and 18.7 hr in early November from Knight & Schleicher (2011) or 18.22 hr around perihelion from Harmon et al. (2011). Note that those ground-based observations have error bars between 0.01 and 0.3 hr. The most robust rotation period at present is from the *EPOXI* spacecraft light curve given in Belton et al. (2013). This light curve gives a spin period of 18.40 hr at the spacecraft's encounter and states that the period was increasing by 1.3 minutes day^{-1}. As the data acquired with the Rosetta filter set spread around one month, it is appropriate to use the midpoint of the observational time interval for this period of time. We extrapolate the rotation period back to the midpoint assuming the rotation period was steadily changing during this time frame. Therefore, the rotation period quoted in this work is 18.11 hr on October 21.5 UT, which refers to the midpoint of the October 10–November 2 data. The zero phase is set at 11:40 UT on 2010 October 10.

In Figure 1, we can see that the morphology of the CN coma extended almost perfectly along the east–west direction in early October and along the north–south direction around Hartley 2's perihelion. The CN images all show clear asymmetries before performing the image enhancement. One of these unprocessed CN images is shown as a contour plot in Figure 1 (top left panel). The variations in the CN jet features in between early October and its perihelion are related to the spin period of the comet nucleus, the changing viewing geometry, and non-principal axis rotation, as has already been reported by Samarasinha et al. (2011), Knight & Schleicher (2011), Lara et al. (2011a) and Waniak et al. (2012). The processed CN images from the observations between October 11 and November 2 revealed two jets in the coma of comet Hartley 2. The CN jet features nearly perpendicular to the Sun-tail direction not only varied smoothly during a night but showed similar morphologies near the comet's perihelion even though the rotational state was different.

We compared the morphologies of the CN jet features with those presented by Knight & Schleicher (2011), and Samarasinha et al. (2011) and found that the CN jet features of Hartley 2 did not show the spiral-like structure in early October but were compatible with the observations obtained by Knight
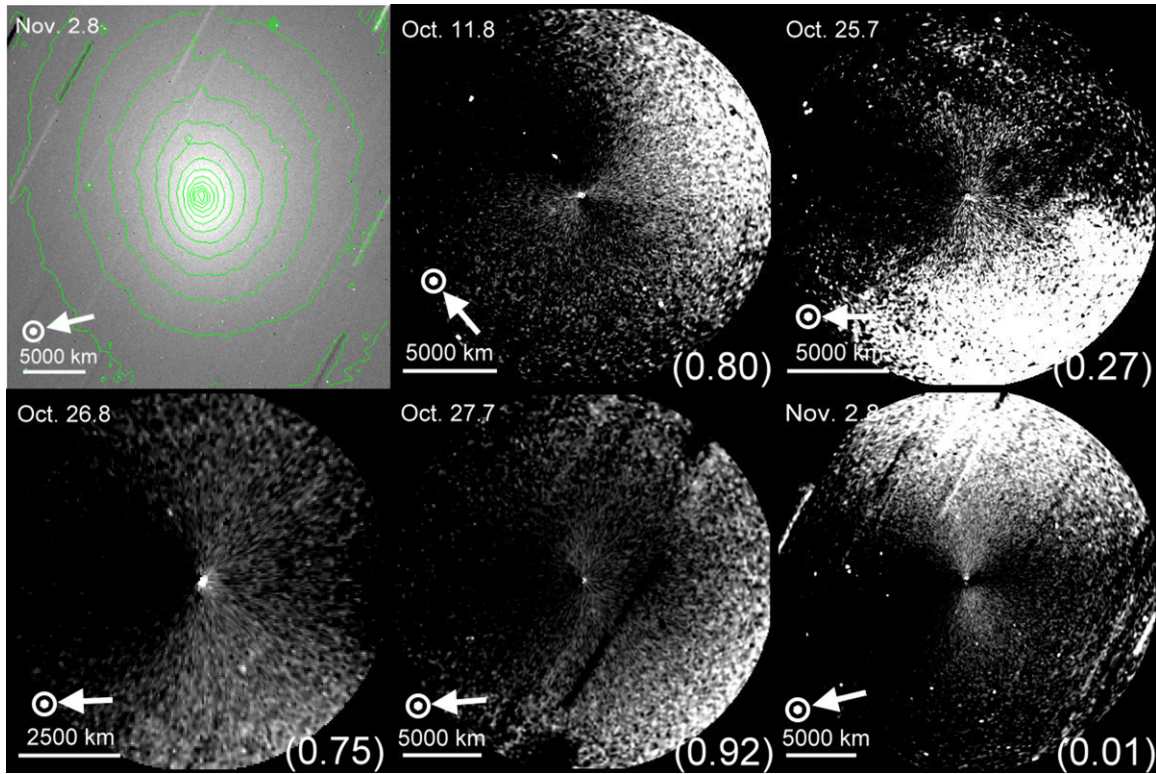
Figure 1. CN images after the dust continuum was removed were enhanced by dividing by an azimuthal median profile. The rotational phase is given in the bottom right corner of each image (see the text for details). The original image (top left) obtained on November 2 is shown with contours overplotted in green. The Sun symbol and arrow indicate the projected direction toward the Sun. North is up, east is to the left. The field of view is $3'.44 \times 3'.44$ and a scale bar is shown at the bottom left corner. The images are centered on the optocenter and the color code stretches to white representing the brightest areas and to black representing the darkest areas.

(A color version of this figure is available in the online journal.)

& Schleicher (2011) and Lara et al. (2011a) in late October. The reason could be the observing geometry, i.e., whether it is observed face-on or side-on. Knight & Schleicher (2011) confirmed this effect from images that revealed face-on spiral structures in August and September. Furthermore, we found these two CN jet features to be asymmetrical. One of them is always brighter than the other, possibly because it is facing toward the Earth. For example, the southern jet of the images obtained from October 25 to October 27 is slightly stronger than the northern jet of those images. Such asymmetrical features have also been reported in earlier works by Samarasinha et al. (2011), Lara et al. (2011a), and Waniak et al. (2012).

3.2. Gas Production Rates

In order to determine the gas production rates, the mean radial emission profiles of CN and C_2 were derived from the continuum-subtracted images. These profiles were also used with the spectra acquired at the Calar Alto Observatory and the Beijing Astronomical Observatory to investigate the CN, C_3, C_2, and NH_2 profiles in the north–south direction and to derive the production rates of these gaseous species. The spectral regions and the subtraction of the underlying continuum in the gas emission bands were done as described by Lara et al. (2001). The conversion of the emission-band fluxes into column densities made use of fluorescence efficiency factors (g-factors) for C_3, C_2, and NH_2 (A'Hearn et al. 1995), whereas the g-factors of the CN molecule were calculated for the heliocentric distance and velocity of 103P/Hartley 2 on every date from the set of values given by Schleicher (2010). The gas production rates were obtained by means of the (Haser 1957) model for isotropic

emission of cometary neutral molecules and their daughter molecules and radicals. The parameter used for the parent velocity is $v_p = 0.85 \, r_h^{-0.5} \, \text{km s}^{-1}$ (Fray et al. 2005) and for the daughter velocity it is $1 \, \text{km s}^{-1}$. For the corresponding set of parameters in the Haser model, we produced theoretical column density profiles for each species by varying the production rate until the best match between observations and theoretical predictions was achieved. The results of nightly averages for Q(CN), Q(C_3), Q(C_2), and Q(NH_2) are summarized in Table 2. Table 2 also contains the average gas production rates obtained from the images acquired in one night together with the aperture size we have considered to derive Q. The variation of production rates seen in multiple measurements during a night were less than 5%; this variation is reflected in the uncertainties in Table 2. We have fewer measurements of Q(C_2) as there were tracking problems at LOT from October 10–11 to October 25–27. Long-slit spectroscopic measurements could provide Q(C_2) at other dates thus spanning larger heliocentric distances.

Our Lulin, BAO and CA results in Table 2 show that there is no significant variation in Q(CN) from mid-October to early November. This result is consistent with the Lara et al. (2011a) and Mumma et al. (2011) results that assumed that HCN is the main parent species of CN and that the expected variation of Q(HCN) around perihelion is not very large. Note that we used the mean radial profile to estimate the gas production rate from the images obtained from Lulin Observatory. However, if we averaged the radial profile in the north–south direction where the CN jet feature exists, the derived Q(CN) would be larger by a factor of two to three compared with the azimuthally averaged radial profile. Figure 2 shows the logarithm of the

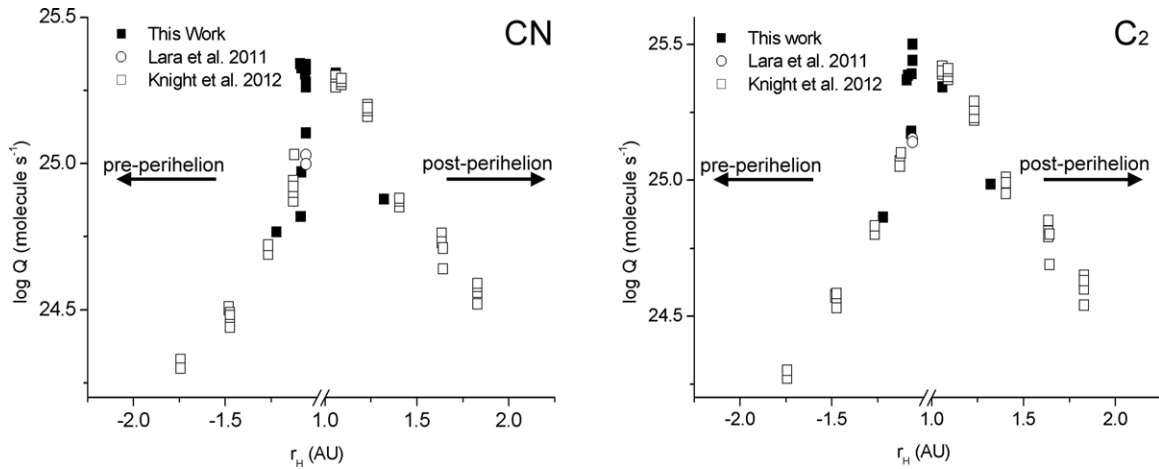**Figure 2.** Log of production rates for CN (left) and C_2 (right) plotted as a function of the heliocentric distance. Different symbols come from different data sets: filled square symbols refer to results presented here; open square symbols are taken from results in Knight & Schleicher (2013); and the open circle symbols come from Lara et al. (2011b). "//" refers to a break in the heliocentric distance from −0.1 AU (pre-perihelion) to 0.99 AU (post-perihelion).

Table 2
Gas Production Rates of Comet 103P/Hartley 2

Date	UT	Observatory	Aperture	CN	C_2	C_3	NH_2	$Q(C_2)/Q(CN)$
Sep 14	00:35–00:57	CA		5.82 ± 0.13	7.28 ± 1.03	0.37 ± 0.05	X	
Oct 9	14:40–17:55	BAO		21.9 ± 4.78	23.4 ± 5.24	4.39 ± 0.94	44.4 ± 9.70	1.07 ± 0.11
Oct 10	12:32–18:45	Lulin	4.01	6.57 ± 0.93	X	X	X	
Oct 11	15:08–19:00	BAO		21.2 ± 3.57	24.3 ± 4.10	4.37 ± 0.74	44.0 ± 7.38	1.15 ± 0.11
Oct 11	13:05–21:08	Lulin	4.00	9.32 ± 1.37	X	X	X	
Oct 18	04:38–05:10	CA		21.4 ± 3.56	14.8 ± 1.57	1.34 ± 0.02	35.2 ± 1.41	0.69 ± 0.04
Oct 18	04:38–05:10	CA		21.2 ± 1.39	15.1 ± 3.99	1.33 ± 0.002	46.9 ± 0.97	0.71 ± 0.29
Oct 22	02:39–03:13	CA		20.2 ± 2.90	24.6 ± 1.57	1.56 ± 0.05	X	1.22 ± 0.05
Oct 25	18:09–18:39	Lulin	3.62	18.2 ± 3.1	X	X	X	
Oct 26	16:09–21:24	Lulin	3.66	20.1 ± 5.4	X	X	X	
Oct 27	16:24–26:56	Lulin	3.82	12.7 ± 2.7	X	X	X	
Oct 28	17:50–21:28	Lulin	3.98	18.9 ± 3.2	27.8 ± 5.3	X	X	1.47 ± 0.17
Oct 29	16:24–21:00	Lulin	3.99	21.8 ± 3.6	31.6 ± 5.4	X	X	1.45 ± 0.15
Nov 2	17:58–20:31	Lulin	4.17	20.3 ± 3.1	22.0 ± 3.2	X	X	1.07 ± 0.10
Dec 26	23:08–00:12	CA		7.54 ± 0.13	9.64 ± 1.6	0.29 ± 0.05	X	1.29 ± 1.23

Notes. Apertures are provided in log units of km. The unit in all gas production rates is 10^{24} molecules s^{-1}.

production rates of CN and C_2 as a function of heliocentric distance (r_h). The data points include those obtained by Lara et al. (2011a), Knight & Schleicher (2013), and the Lulin and CA results (this work) for pre-perihelion and post-perihelion observations during the 2010 apparition. We used linear fitting in log–log space to estimate the slope of the r_h dependence of the gas production rate, $Q \sim r_h^{-\alpha}$. The slopes (α) of CN and C_2 are 4.57 and 4.84 before perihelion and 3.21 and 3.42 after perihelion, respectively. These slopes are significantly steeper than the average value estimated for Jupiter-family comets, i.e., $Q(\text{gas}) \sim r_h^{-2.7}$ (A'Hearn et al. 1995). In addition, the average C_2-to-CN production rate ratio is 0.7–1.5, classifying 103P/Hartley 2 as typical in terms of cometary chemistry as defined by A'Hearn et al. (1995). Our measurement is consistent with results from spectroscopic observations (Lara et al. 2011a) and narrowband photometry observations (Knight & Schleicher 2013).

4. DUST COMA MORPHOLOGY AND PROPERTIES

4.1. The Jet Feature in the Dust Coma

We describe the morphology and evolution of the coma structures that can be treated with routine procedures, i.e., the Larson–Sekanina algorithm (Larson & Sekanina 1984). In case of doubt, we used additional techniques, such as azimuthal median profile division and the Adaptive Laplace filter (Böhnhardt & Birkle 1994), to clearly separate morphological features from artifacts. Figure 3 compares observations from October 11 of the jet structure and dust tail using three different image enhancement methods: (1) Larson–Sekanina filtering, (2) the azimuthal median profile, and (3) adaptive Laplace filtering. In spite of some differences in their appearances, the presence of two jets in the sunward quarter is common to all numerical treatments. It is therefore clear that the jet features are real and not artifacts associated with the image processing procedures.

Figure 4 is a summary of the R-band images enhanced by the Larson–Sekanina filtering method to bring out the inhomogeneous structures in the dust coma of 103P/Hartley 2. It can be seen that from 2010 April until July no clear sign of dust features could be found. However, beginning on August 1, a dust tail with a diffuse structure (labeled T in Figure 4) began to appear in the anti-sunward direction. On September 29, a short jet (indicated by arrows in Figure 4) in the sunward direction can be seen. Hereafter, this sunward jet feature can be detected in all our images obtained at Lulin and Calar Alto observatories. It is interesting to note that two distinct sunward dust structures
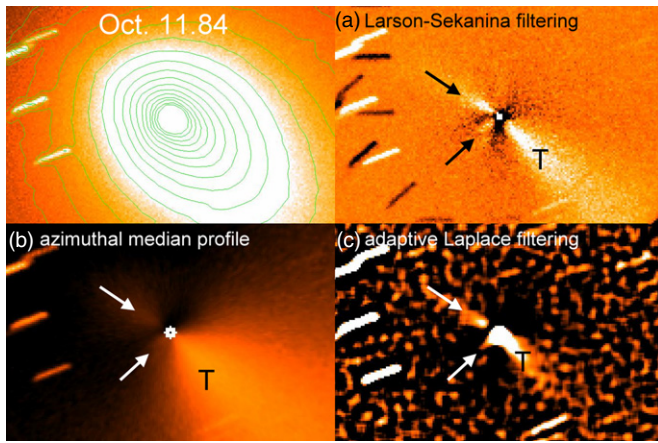
Figure 3. Image of comet 103P/Hartley 2 obtained on 2010 October 11 with the *R* broadband filter. In the top left corner, a contour plot of the original image is shown. In (a) we display the same image after Larson–Sekanina filtering, in (b) the image is divided by an azimuthal median profile, and in (c) the adaptive-Laplace technique has been applied. In all of these images, two jet features are visible. North is up, east is to the left. The field of view is $2'.92 \times 1'.94$, corresponding to 9200×6100 km at the comet distance. The images are centered on the nucleus, the arrows point out the jets, T labels the tail, and the streaks are trailed stars. The negatives of the star trails in panel A are the artifacts of the resulting image being subtracted using a combination of a 15° counterclockwise rotation and a 15° clockwise rotation. As the images are normalized, the brightness scales from 0.95 to 1.05.

(A color version of this figure is available in the online journal.)

are visible after October 29 lasting until November 2. Around the same time, from November 2 to November 4, Mueller et al. (2013) also reported seeing two separate continuum features in the sunward direction. Afterward, only a single jet could be seen in the sunward direction. This jet became fainter and fainter as Hartley 2's heliocentric and geocentric distances increased. The sunward jet features showed relatively little variation during a night but their shape and PA slightly changed from night to night until October 11 when two distinct jet features apparently emerged from the sunward direction (Figure 5). In order to examine the existence of this extremely faint jet feature and to distinguish it from the trail of a background star, we transformed the enhanced image into polar coordinates ρ–θ where ρ is the projected cometocentric distance from the nucleus and θ is the azimuth (PA). At several distances ρ from the nucleus, we analyzed the resulting azimuthal profile. In Figure 5 (right panel) we show the azimuthal profile at $\rho = 5000$ km. It can be seen that this faint jet (referred to as the main feature in the figure) appears on October 11.76 and persists until October 11.87, that is, ∼0.7 hr later (bottom panel in Figure 5). It points toward the Sun and it does not display significant changes. On October 11.84, a new faint feature appears nearly perpendicularly to the Sun-comet line. It is interesting to note that the PA of the secondary jet is roughly the same as that of the CN jet features shown in Figure 1 (pointing to the eastsouth direction in the top middle panel). At first, one could think that icy grains mixed with the dust grains of this weaker jet could provide the partial fuel to the CN gas jet. However, the gas jets persist for most of a rotation period (Knight & Schleicher 2011; Samarasinha et al. 2011) and are clearly being released over an extended period of time as the nucleus rotates. Thus, the CN jets cannot mainly come from this faint jet feature if it is only active for a few hours as found here. That switching phenomenon may also be explained as a projection effect due to the comet nucleus rotation.
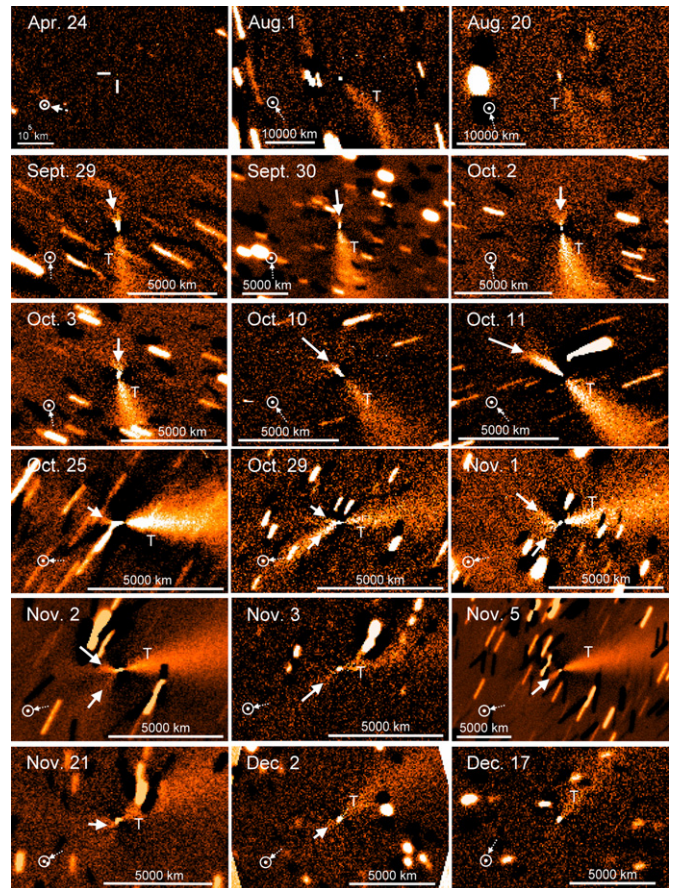

Figure 4. Images of comet 103P/Hartley 2 acquired with the *R*-band filter and enhanced by the Larson–Sekanina algorithm. The dust sunward jet feature sometimes appears as a straight jet but sometimes it shows multiple jet features during a night. The jet showed minimal change in shape, position angle, and extent from night to night. The Sun symbol and arrow indicate the projected direction toward the Sun. North is up, east is to the left. The field of view is $2'.92 \times 1'.94$ and the scale bar is shown in the bottom corner. All images are centered on the nucleus, arrows point out the jets, and T represents the tail.

(A color version of this figure is available in the online journal.)

On October 28 and 29, we obtained a series of images from Lulin and Calar Alto observatories that provide insight into how the sunward feature evolved throughout ∼1.4 rotation cycles. Representative images from these nights are shown in Figure 6, with each panel enhanced by the Larson–Sekanina filtering method. Note that the PA of the Sun during these two days is near 97°. Setting the zero phase at 11:40 UT on October 10 and using a period of 18.11 hr (see Section 3), the rotational phase can be easily estimated in these three images (see the bottom right corner of the panels in Figure 6). A dust jet (labeled J and marked with an arrow in Figure 6) can be seen in the sunward direction; its shape slightly changes as the rotational phase changes from 0.22 (October 28.68 UT) to 0.82 (October 29.13 UT). Thirteen hours later (rotational phase of 0.57, October 29.70 UT) two dust jet features emanating in the sunward direction can be seen. One of them, labeled J_1, is close to the position of Sun (PA $\sim$ 85°) and the other, labeled J_2, lies at PA $\sim$ 130°. We consider the possibility that the J_1 feature might have the same source region as the jets in the previous two images (October 28.68 and October 29.13), since all the jets have similar PAs. Under this assumption, the J_2 feature is new. Another possibility is that the J_1 feature might be associated with the cometary rotational effect, i.e., local sunrise accompanied by a temperature increase
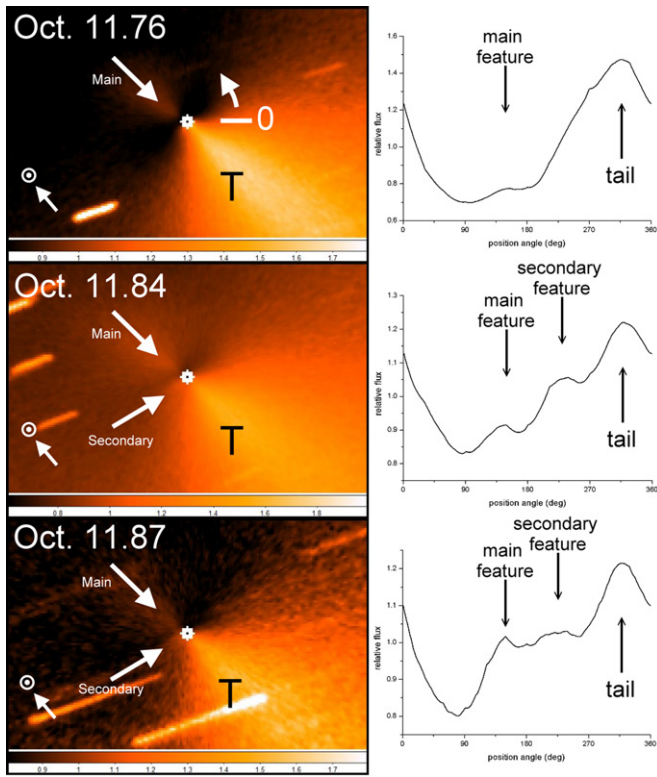
Figure 5. Dust jet features and tail enhanced by an azimuthal median profile (left panels) and the corresponding azimuthal profiles obtained at $\rho \sim 5000$ km (right panels). A sunward dust jet feature is revealed in the broadband R filter on October 11.76 UT (top panel). Two faint dust jet features are detected using both broadband R (middle panel) and narrowband red-continuum filters (bottom panel) on October 11.84 UT and 11.87 UT, respectively. The straight jet pointing toward the Sun (main feature) and the weaker one pointing nearly perpendicular to the Sun–nucleus direction (secondary feature) are marked in the graphs. Position angle is measured from north (up) in the counterclockwise direction (top left panel). In the left panels, all images are centered on the nucleus, with arrows indicating the jets and T indicating the dust tail. North is up, east is to the left. The field of view is $2'.92 \times 1'.94$, corresponding to 9200×6100 km at the comet distance; the Sun symbol and the corresponding arrow indicate the projected direction toward the Sun.

(A color version of this figure is available in the online journal.)
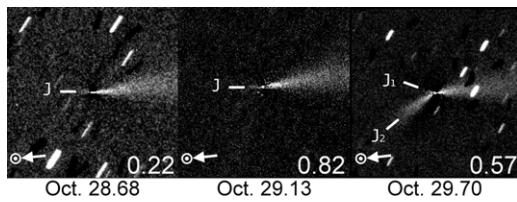

Figure 6. Time sequence of images of the comet 103P/Hartley 2 acquired from the Lulin (left and right) and CA (middle) observatories. Dust jet features are enhanced by Larson–Sekanina filtering. The rotational phase is given at the bottom right corner of each image. North is up, east is to the left. The field of view is $3'.8 \times 3'.8$ and all images are centered on the nucleus. J, J_1, and J_2 refer to the jets and the Sun symbol and arrow indicate the projected direction toward the Sun.

turns that jet on. This localized temperature difference in the regions of the waist and the Sun-lit end of the nucleus have been addressed by Belton et al. (2013). The J_2 feature, which has a collimated shape, is the persistent feature we detected on October 28.68 and October 29.13, although its PA and shape changed between those two dates. We note that the J_2 feature is brighter than the J_1 feature. This higher intensity could be related to dusty ice or to an outburst from the surface of the comet nucleus. To understand which of these processes is responsible
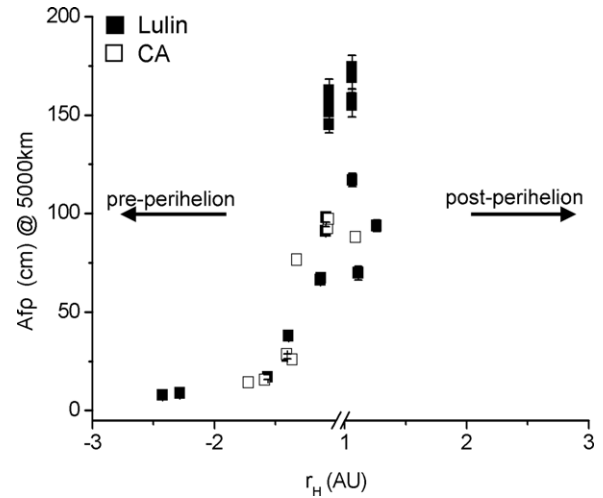

Figure 7. Afρ variation as a function of heliocentric distance both pre- and post-perihelion. Filled squares indicate the results obtained from the Lulin Observatory (LOT) and open squares pertain to the data from the Calar Alto Observatory. "//" refers to the break in heliocentric distance from -0.1 AU (pre-perihelion) to 0.99 AU (post-perihelion). The error bars are not clearly seen in this figure because they are smaller than 5%.

for the differential brightening, our images need to be interpreted in the context of a larger image series that displays the time evolution of the jet structure over two or more rotational periods.

On the tailward side, only the dust tail was readily visible starting in 2010 August. The dust tail was found to point approximately in the antisolar direction. As expected, it appears to be curved slightly counterclockwise.

4.2. The Properties of the Dust Coma

We used Afρ (A'Hearn et al. 1984) to characterize the dust activity of the comet. The derived values acquired with the broadband R filter from 2010 April to November are presented in Figure 7. Except for the night of October 29, the average values estimated every photometric night were all measured within a projected distance of 5000 km. Note that Afρ shows a weak dependence on ρ, the projected cometocentric distance from the nucleus, from 5000 km to 20,000 km and that the variation was found to be less than approx. 5%–8%. The reason why we used 5000 km for the uniform radius was to reduce the influence of star trails in the FOV. The $Af\rho$ values steadily increased with decreasing heliocentric distance, although there was not a noticeable increase when the second jet appeared on October 11.64 UT or at perihelion. The $Af\rho$ value on October 29.77–29.85 UT increased from 155 cm to 174 cm in two hours, and at the same time the dust jet seen in Figure 6 (right panel) was more prominent on this night than on any of the other nights. A relatively weak secondary jet feature was also detected. Possible causes for this deviation might include changes in the physical properties of the grains as they traveled outward (i.e., loss of volatiles or fragmentation), the action of solar radiation pressure modifying the straight trajectories of small particles inside the FOV, or a long-lasting population of large particles (Schleicher et al. 1998). Furthermore, the power-law index of the r_h dependence for the dust, Afρ (5000 km), is -3.75 ± 0.45 before perihelion and -3.44 ± 1.20 post-perihelion. This result is completely consistent with the result of Knight & Schleicher (2013) when using A(θ)fρ.

The derived Afρ values for the narrowband filter can be used to estimate the color of the cometary dust (Jewitt & Meech 1987)
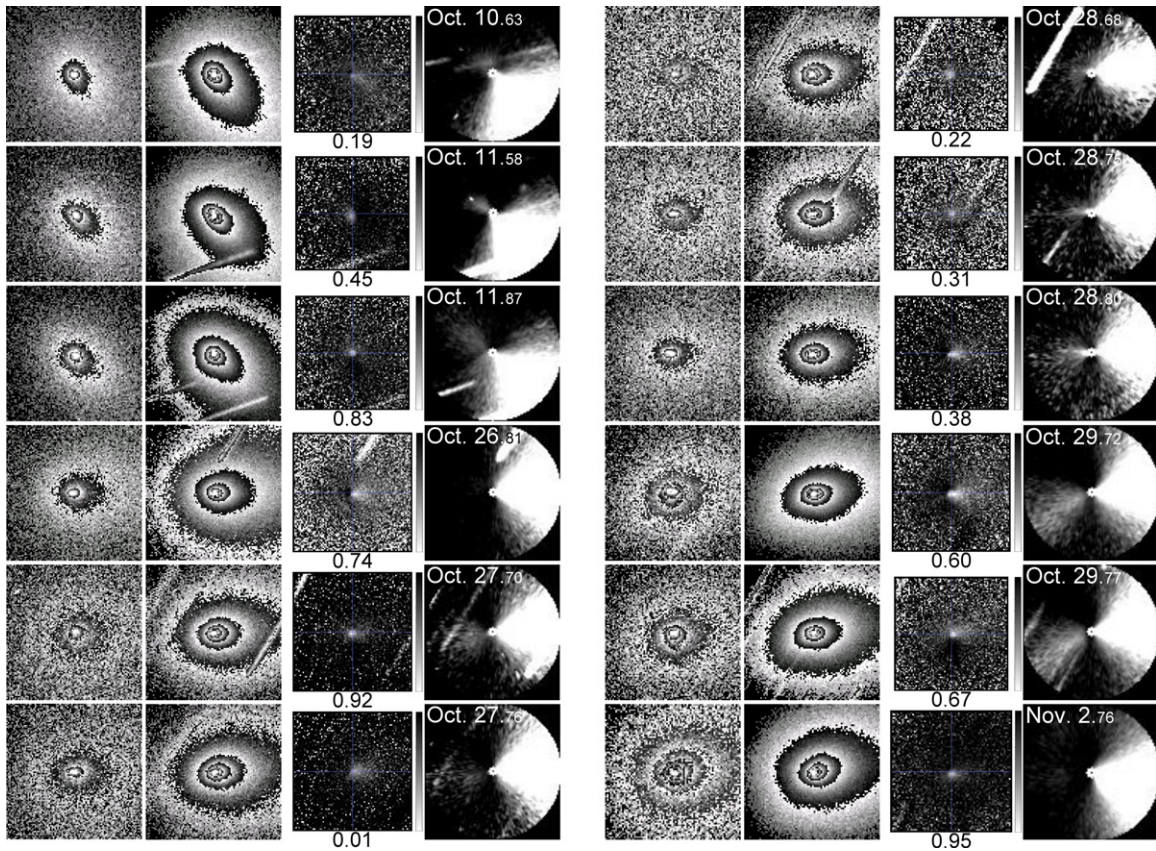
Figure 8. Jet activity and dust color of the coma of 103P/Hartley 2. The first two columns are images acquired with the blue continuum filter centered at 443 nm (BC) and with red continuum filter centered at 684 nm (RC), respectively. The third column shows the dust reddening computed with Equation (1). The color bar stretches from 0% (black) to 50% (white)/100 nm. The fourth column displays the ring-masking images obtained by subtracting the RC images from an image generated with the azimuthal average profile. North is up, east is to the left. The field of view is about $40'' \times 40''$, corresponding to 1800 km–2200 km at the comet distance depending on the different comet heliocentric distances.

Table 3
The Dust Color Averaged within the Innermost 5000 km of the Coma

Date	Color (%/100 nm)
Oct 10	9.40 ± 0.82
Oct 11	11.50 ± 0.934
Oct 25	5.06 ± 0.78
Oct 26	6.36 ± 0.82
Oct 27	6.43 ± 0.87
Oct 28	11.07 ± 0.83
Oct 29	10.01 ± 0.83
Nov 2	5.56 ± 0.88

as the normalized gradient of the $Af\rho$ product between the blue (BC, $\lambda_0 = 4430$ Å) and red (RC, $\lambda_0 = 6840$ Å) continuum filters. The dust color can be converted to a percentage of reddening per 1,000 Å and is defined by the following relation:

$$\text{color} = \frac{RC_{Af\rho} - BC_{Af\rho}}{6840 - 4430} \frac{2000}{RC_{Af\rho} + BC_{Af\rho}}. \quad (1)$$

The summarized results in Table 3 indicate that the average dust color within the innermost 5000 km of the coma did not appear to vary significantly with heliocentric distance. This behavior of the averaging dust color seems to indicate that the innermost coma does not introduce significant changes in the size distribution and/or overall properties of dust grains. As we found a jet feature that switches on and off from our images in Figures 4–6, we analyzed all the flux-calibrated images acquired

with the BC and RC narrowband filters instead of integrating the whole flux in the innermost 5000 km. The resulting two-dimensional dust color map can be seen in Figure 8 (the third column). Figure 8 displays the dust coma of comet 103P/Hartley 2 from October 10 to November 2 imaged in the BC and RC narrowband filters (first two columns), the dust color map (the third column) and the azimuthal median profile subtracted RC filter images (the fourth column) displaying the jet activity in the dust coma. The data presented here pertaining to October and November indicate extreme dust reddening, with a normalized color ~30%–45% within a radius of ~50–100 km measured from the optocenter of the images. This red dust could be associated with strong jet activity. The sunward jet feature might give rise to higher dust abundances at closer cometocentric distances (i.e., nearer the optocenter). These dust grains are initially large with a reddening of ~30%–40%/1,000 Å; while traveling out, they split up and show less reddening at ~500 km with a dust reddening of ~10%–15%. In comparison with the tailward direction, the color variation is 5%–10%. The decrease in the dust reddening means that the optical properties of the dust grains change as the dust grains move outward. The decrease in the reddening could be also associated with an outburst (Bonev et al. 2002). A possible explanation for the color variation is that the larger dust grains mixed with the icy grains dominate the scattering behavior at close distance around the nucleus. When these larger dust grains move outward, they break up or sublimate into small submicron particles, resulting in a bluer continuum due to their smaller sizes (Lara et al. 2011a).

5. SUMMARY

We observed the comet Hartley 2 at the Lulin Observatory in Taiwan, the Calar Alto Observatory in Spain, and the Beijing Astronomical Observatory in China, from 2010 April to December using both broadband and narrowband filters, and long-slit spectrophotometry. The results are summarized below.

1. *CN morphology.* The processed CN images revealed two asymmetric jet features in the coma of comet Hartley 2. The CN jet features detected in the images presented here did not show the spiral-like structure seen by other authors at earlier dates due to a different observing geometry. One of these CN jet features always shows a higher intensity than the other, possibly because it is facing toward the Earth.

2. *Gas production rates.* Our Lulin, BAO, and CA results show that there is no significant variation of Q(CN) from mid-October to early November. The power-law slopes of the heliocentric distance of the gas production rate of CN and C_2 are -4.57 and -4.84 before perihelion and -3.21 and -3.42 after perihelion. The average C_2-to-CN production rate ratio is $0.7 \sim 1.5$, consistent with 103P/Hartley 2 being typical in terms of C_2 enrichment.

3. *Dust morphology.* The sunward jet feature was first detected in images acquired at the end of 2010 September. This sunward jet does not seem to be permanent. Instead, its morphology varies with time and two distinct jet features are found on October 11 and after October 29 until November 2.

4. *Afρ and dust color.* The power-law r_h dependence of the dust production rate, Afρ (5000 km), is -3.75 ± 0.45 before perihelion and -3.44 ± 1.20 during post-perihelion. The higher dust reddening found around the optocenter could be associated with a stronger jet activity. The dust color is getting bluer outward along the sunward jet, implying that the optical properties of the dust grains change with ρ. The average dust color did not appear to vary significantly when the heliocentric distance decreased to perihelion.

REFERENCES

A'Hearn, M. F., Belton, M. J. S., Delamere, W. A., et al. 2011, Sci, 332, 1396
A'Hearn, M. F., Millis, R. L., Schleicher, D. G., Osip, D. J., & Birch, P. V. 1995, Icar, 118, 223
A'Hearn, M. F., Schleicher, D. G., Millis, R. L., Feldman, P. D., & Thompson, D. T. 1984, AJ, 89, 579
Belton, M. J. S., Thomas, P., Li, J.-Y., et al. 2013, Icar, 222, 595
Böhnhardt, H., & Birkle, K. 1994, A&A, 107, 101
Bonev, T., Jockers, K., Petrova, E., et al. 2002, Icar, 160, 419
Drahus, M., Jewitt, D., Guilbert-Lepoutre, A., et al. 2011, ApJL, 734, L4
Fray, N., Bénilan, Y., Cottin, H., Gazeau, M.-C., & Crovisier, J. 2005, P&SS, 53, 1243
Harmon, J. K., Nolan, M. C., Howell, E. S., Giorgini, J. D., & Taylor, P. A. 2011, ApJL, 734, L2
Haser, L. 1957, BSRSL, 43, 740
Jewitt, D. C., & Meech, K. J. 1987, ApJ, 317, 992
Knight, M. M., & Schleicher, D. G. 2011, AJ, 141, 183
Knight, M. M., & Schleicher, D. G. 2013, Icar, 222, 691
Lara, L. M., Lin, Z.-Y., & Meech, K. 2011a, A&A, 532, 87L
Lara, L. M., Lin, Z.-Y., Rodrigo, R., & Ip, W.-H. 2011b, A&A, 525, 36L
Lara, L. M., Schulz, R., Stüwe, J. A., & Tozzi, G. P. 2001, Icar, 150, 124
Larson, S. M., & Sekanina, Z. 1984, AJ, 89, 571
Lin, Z.-Y., Chang, C.-P., & Ip, W.-H. 2007a, AJ, 133, 1861
Lin, Z.-Y., Lara, L. M., Vincent, J. B., & Ip, W.-H. 2012, A&A, 537, 101L
Lin, Z.-Y., Weiler, M., Rauer, H., & Ip, W.-H. 2007b, A&A, 469, 771
Meech, K. J., A'Hearn, M. F., Adams, J. A., et al. 2011, ApJL, 734, L1
Mueller, B. E. A., Samarasinha, H., Farnham, T. L., & A'Hearn, M. F. 2013, Icar, 222, 799
Mumma, M. J., Bonev, B. P., Villanueva, G. L., et al. 2011, ApJL, 734, L7
Samarasinha, N. H., Mueller, B. E. A., A'Hearn, M. F., Farnham, T. L., & Gersch, A. 2011, ApJL, 734, L3
Schleicher, D. G. 2010, AJ, 140, 973
Schleicher, D. G., Millis, R. L., & Birch, P. V. 1998, Icar, 132, 397
Waniak, W., Borisov, G., Drahus, M., & Bonev, T. 2012, A&A, 543, A32